Downloaded from orbit.dtu.dk on: Dec 17, 2017

Technical University of Denmark

Temporal evolution of confined fast-ion velocity distributions measured by collective Thomson scattering in TEXTOR

Nielsen, Stefan Kragh; Bindslev, Henrik; Porte, L.; Hoekzema, J.A.; Korsholm, Søren Bang; Leipold, Frank; Meo, Fernando; Michelsen, Poul; Michelsen, Susanne; Oosterbeek, J.W.; Tsakadze, Erekle; Wassenhove, G. Van; Westerhof, E.; Woskov, P.

Published in:
Physical Review E (Statistical, Nonlinear, and Soft Matter Physics)

Link to article, DOI:
10.1103/PhysRevE.77.016407

Publication date:
2008

Document Version
Publisher's PDF, also known as Version of record

Link back to DTU Orbit

Citation (APA):
Nielsen, S. K., Bindslev, H., Porte, L., Hoekzema, J. A., Korsholm, S. B., Leipold, F., ... Woskov, P. (2008). Temporal evolution of confined fast-ion velocity distributions measured by collective Thomson scattering in TEXTOR. Physical Review E (Statistical, Nonlinear, and Soft Matter Physics), 77(1), 016407. DOI: 10.1103/PhysRevE.77.016407

DTU Library
Technical Information Center of Denmark

General rights
Copyright and moral rights for the publications made accessible in the public portal are retained by the authors and/or other copyright owners and it is a condition of accessing publications that users recognise and abide by the legal requirements associated with these rights.

- Users may download and print one copy of any publication from the public portal for the purpose of private study or research.
- You may not further distribute the material or use it for any profit-making activity or commercial gain
- You may freely distribute the URL identifying the publication in the public portal

If you believe that this document breaches copyright please contact us providing details, and we will remove access to the work immediately and investigate your claim.

Temporal evolution of confined fast-ion velocity distributions measured by collective Thomson scattering in TEXTOR

S. K. Nielsen,[1,2,*] H. Bindslev,[1] L. Porte,[5] J. A. Hoekzema,[3] S. B. Korsholm,[1] F. Leipold,[1] F. Meo,[1] P. K. Michelsen,[1] S. Michelsen,[1] J. W. Oosterbeek,[3] E. L. Tsakadze,[1,†] G. Van Wassenhove,[6] E. Westerhof,[4] and P. Woskov[2]

[1]*Association EURATOM-Risø National Laboratory, Technical University of Denmark, DK-4000 Roskilde, Denmark*

[2]*MIT Plasma Science and Fusion Center, Cambridge, Massachusetts 02139, USA*

[3]*Forschungszentrum Jülich GmbH, Institut für Energieforschung–Plasmaphysik, EURATOM Association, Trilateral Euregio Cluster, D-52424 Jülich, Germany*

[4]*FOM-Insitute for Plasma Physics Rijnhuizen, Association EURATOM-FOM, Trilateral Euregio Cluster, The Netherlands*

[5]*CRPP, Association EURATOM-Confédération Suisse, EPFL, CH-1015 Lausanne, Switzerland*

[6]*Ecole Royale Militaire-Koninklijke Militaire School, Laboratory for Plasma Physics, Association EURATOM-Belgian State, Trilateral Euregio Cluster, B-1000, Brusssels, Belgium*

(Received 15 July 2007; published 29 January 2008)

Fast ions created in the fusion processes will provide up to 70% of the heating in ITER. To optimize heating and current drive in magnetically confined plasmas insight into fast-ion dynamics is important. First measurements of such dynamics by collective Thomson scattering (CTS) were recently reported [Bindslev *et al.*, Phys. Rev. Lett. **97**, 205005 2006]. Here we extend the discussion of these results which were obtained at the TEXTOR tokamak. The fast ions are generated by neutral-beam injection and ion-cyclotron resonance heating. The CTS system uses 100–150 kW of 110-GHz gyrotron probing radiation which scatters off the collective plasma fluctuations driven by the fast-ion motion. The technique measures the projected one-dimensional velocity distribution of confined fast ions in the scattering volume where the probe and receiver beams cross. By shifting the scattering volume a number of scattering locations and different resolved velocity components can be measured. The temporal resolution is 4 ms while the spatial resolution is ~10 cm depending on the scattering geometry. Fast-ion velocity distributions in a variety of scenarios are measured, including the evolution of the velocity distribution after turnoff of the ion heating. These results are in close agreement with numerical simulations.

DOI: 10.1103/PhysRevE.77.016407 PACS number(s): 52.25.Os, 52.70.Gw, 52.40.Db, 52.50.Gj

I. INTRODUCTION

In future tokamak experiments, such as ITER, and in future fusion power plants, the main source of heating will come from the plasma itself in the form of fast α particles produced in D-T fusion reactions. These fast α particles must transfer their energy to the bulk plasma before they are expelled from the plasma. It is important to understand the fast-ion dynamics, especially the interaction with plasma instabilities, to develop scenarios which avoid premature expulsion of the fusion α's. Fast ions can, for instance, be prematurely ejected by Alfvén modes driven by the fast ions [1–6]. Also sawteeth are reported to redistribute fast ions and be influenced by the fast ions [7–11].

As a challenge to current theory and as guidance for the further development of our understanding of fast-ion dynamics, experimental measurements of confined fast ions resolved in time, space, and velocity are needed. Collective Thomson scattering (CTS) can, as demonstrated here, provide such measurements. The fast-ion CTS diagnostic is based on the scattering of electromagnetic waves off microscopic fluctuations, principally in the electron distribution, driven by ion motion [12–16]. By using CTS it is possible to measure the localized confined fast-ion velocity distribution projected onto a given direction depending on the scattering geometry. CTS has also been used in magnetically confined plasmas as an ion temperature diagnostic using far-infrared radiation [17] and later using millimeter-wave gyrotron radiation [18–20]. Fast-ion data from CTS were first obtained at JET [21], and recently first measurements resolving fast-ion dynamics by CTS were made at TEXTOR [22].

This paper presents detailed measurements of the fast-ion velocity distribution function in the TEXTOR tokamak measured by CTS and is an extension of the discussion in [22]. In Sec. II the principles of CTS are described; Secs. III and IV describe the diagnostic system, show examples of raw data, and provide evidence of the CTS origin of the measured data. Section V deals with the analysis of these data, and Sec. VI discusses the inferred velocity distribution. Experimental measurements of the evolution of the fast-ion velocity distribution after the ion heating was turned off are compared with simulations in Sec. VII. Conclusions are drawn in Sec. VIII.

II. CTS THEORY

In CTS a probing beam of radiation is incident on the plasma and a receiver beam collects radiation scattered from the probe beam by fluctuations in the plasma. The geometry of these beams (scattering geometry) determines which velocity component is resolved, where the measurement is

*stefan.kragh.nielsen@risoe.dk

†Present address: NanonA/S, Priorparken 878, DK-2605 Broendby, Denmark.

 ©2008 The American Physical Society

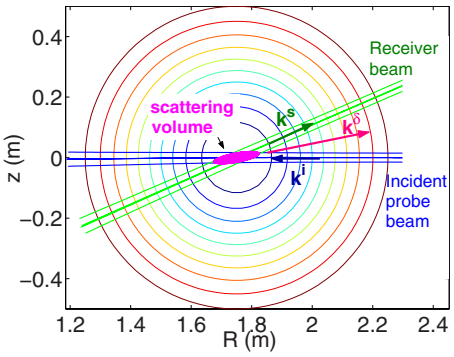

FIG. 1. (Color online) CTS scattering geometry in the TEXTOR tokamak. The probe enters the plasma in the horizontal midplane and the first receiver mirror is located ~20 cm above. The resolved fluctuation wave vector $\mathbf{k}^\delta = \mathbf{k}^s - \mathbf{k}^i$ is generally pointing towards the launch and receiver mirrors for the back scattering geometry used on TEXTOR.

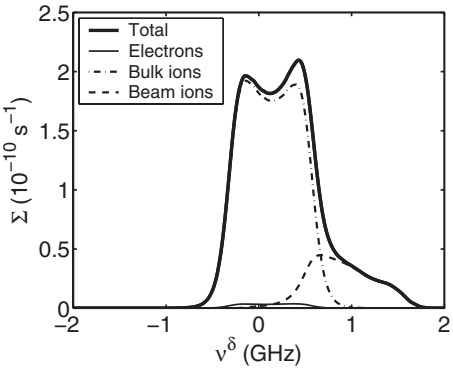

FIG. 2. Theoretical scattering function Σ for a neutral-beam-heated TEXTOR plasma. The resolved velocity component makes an angle of 160° to the static magnetic field. The plasma parameters are $n_e = 3\times10^{19}$ m^{-3}, $T_e = T_i = 2$ keV, $n_D = 2.5\times10^{19}$ m^{-3}, $n_H = 2\times10^{18}$ m^{-3}, and $n_{\text{beam ion}} = 3\times10^{18}$ m^{-3}.

taken spatially, and with what spatial resolution. The latter are given by the location and the extent of the scattering volume which is the spatial region where the probe and receiver beams overlap. In Fig. 1 we show a poloidal map of an example of a scattering geometry in TEXTOR, showing both the scattering volume and the wave vectors involved. The wave vector and frequency of the resolved fluctuation are given by $(\omega^\delta, \mathbf{k}^\delta) = (\omega^s - \omega^i, \mathbf{k}^s - \mathbf{k}^i)$, where superscripts "i" and "s" refer to incident and scattered, respectively.

The spectral power density of the scattered radiation collected by the CTS receiver is given by the equation of transfer [15,16]:

$$\frac{\partial P^s}{\partial \nu^s} = P^i O_b (\lambda_0^i)^2 r_e^2 n_e \frac{1}{2\pi} \Sigma, \tag{1}$$

where P^s and ν^s are the power and the frequency of the received scattered radiation, P^i is the incident power, O_b is the beam overlap, λ_0^i is the vacuum wavelength of the incident probing radiation, r_e is the classical electron radius, n_e is the electron density, and Σ is the scattering function. The beam overlap is the volume integral of the product of the normalized probe and receiver intensity. Σ accounts for the microscopic fluctuations and the efficiency with which these fluctuations scatter the probe radiation into the received radiation [15]. The power density of the received scattered radiation is proportional to the scattering function which is the main term accounting for the functional variation with respect to the frequency, ν^s, of the received radiation. O_b can also have a small dependence on ν^s because of dispersion. This is neglected here. The scattering function further accounts for the functional variations with plasma parameters and the probing frequency. Together with O_b it also accounts for dependence on scattering geometry. Extraction of ion information from Thomson scattering requires that the scattering be dominantly off collective fluctuations, which implies $\alpha \equiv (|\mathbf{k}^\delta|\lambda_D)^{-1} > 1$. Here α is the Salpeter parameter and λ_D is the Debye length. Thus fluctuation scale lengths longer than the Debye length are resolved by CTS. The scattering function can be divided into parts due to fluctuations driven by the motion of, respectively, bulk ions, i, electrons, e, and fast ions, α:

$$\Sigma = \sum_{j=i,e,\alpha} \Sigma_j. \tag{2}$$

The dependence of the quantity Σ_α on the fast-ion velocity distribution is principally on the projection of the distribution onto $\mathbf{k}^\delta$—that is, $f_\alpha^{1D}(u) = \int \delta(u - \mathbf{v}\cdot\mathbf{k}^\delta/k^\delta) f_\alpha(\mathbf{v}) d\mathbf{v}$, where $f_\alpha(\mathbf{v})$ is the fast-ion velocity distribution. Σ_α accounts for the fluctuations, principally in the electron distribution, driven by the motions of the fast ions. The drive of these fluctuations can be pictured as a swan on a lake leaving a depression in the water and drawing a wake, the swan being the fast ion and the water the electron distribution. The depression corresponds to the Debye shielding surrounding the ion while the wake corresponds to weakly damped waves excited by resonant interaction with the ion motion. The frequency ω^δ of a particular wave vector component $\mathbf{k}^\delta$ of the fluctuations driven by a particular ion is approximately given by $\nu^\delta = \mathbf{v}_{\text{ion}}\cdot\mathbf{k}^\delta/2\pi$, where $\mathbf{v}_{\text{ion}}$ is the velocity of the ion setting up the fluctuation. A typical scattering function for the TEXTOR CTS system is shown in Fig. 2. Here the resolved wave vector $\mathbf{k}^\delta$ is at an angle of 160° to the static magnetic field and the fast-ion population is the computed steady-state distribution resulting from a deuterium neutral beam injected with a particle energy of 50 keV.

It can be seen that for positive frequencies a contribution from the fast ions is present while no contribution is noted for negative frequencies. This is because the beam ions modeled here are born with a velocity component antiparallel to the magnetic field and hence $\mathbf{k}^\delta \cdot \mathbf{v}_{\text{beam ion}} > 0$.

III. METHOD

The CTS system at the TEXTOR tokamak ($R = 1.75$ m, $a = 0.45$ m) uses probe radiation at 110 GHz from a gyrotron operated at ~100–150 kW in short pulses with an integrated on-time of at most 200 ms. The probe radiation is pulsed to distinguish the CTS signal from background ECE emissions.

For CTS operation with this gyrotron the tokamak toroidal magnetic field on the magnetic axis is set at ~2.6 T so that the fundamental and second harmonics of the cold electron cyclotron resonance at 110 GHz are located outside the plasma on the high-field side and low-field side, respectively ($R=1.16$ m, $R=2.32$ m). During scattering experiments it is important to operate without a strong resonance in the plasma since this would give rise to significant electron heating when the gyrotron probe radiation is fired into the plasma and hence result in an increase in the electron cyclotron emission (ECE) level, which in this case would be indistinguishable from the scattered CTS signal. Furthermore, the signal-to-noise ratio would decrease significantly since the main contributor to the noise is ECE from the plasma.

The spectral power density of the CTS signal in the frequency range of interest for fast ion dynamics is on the order of 1–10 eV. This has to be compared to the background ECE which is in the range 10–100 eV when the cold ECE resonances are outside the plasma. To separate the scattered signal from the ECE background the gyrotron is modulated, typically with a 50% duty cycle, 2 ms on, 2 ms off, giving a temporal resolution of 4 ms. The gyrotron beam enters the plasma from the low-field side in the horizontal midplane and the launch direction may be altered by a steerable mirror near the plasma. Likewise, the orientation of the receiver beam is controlled by a movable mirror placed on the low-field side approximately 20 cm above the entry of the probe beam as seen in Fig. 1. The received scattered radiation is detected using a hetrodyne receiver upgraded to 42 spectral channels with bandwidths from 80 MHz to 750 MHz, giving complete coverage from 107 GHz to 113 GHz [23]. A notch filter of 120 dB rejection over a 200-MHz bandwidth is used to reduce stray radiation at the gyrotron frequency. A big effort has been made to find gyrotron operating scenarios with a spectrally pure output without spurious modes [24]. However, during the gyrotron turn-on and turn-off phases the gyrotron frequency is unstable and may be outside the range of the notch. To avoid significant gyrotron stray light reaching the receiver electronics, a pin switch is used to attenuate the signal for about 0.1 ms during the gyrotron switching phases. The diagnostic is calibrated using thermal emission from the empty vacuum vessel and ECE. Further details on the diagnostic and its upgrades can be found in [23–27]. All data discussed here are from the upgraded system except data from discharge No. 89509.

In Fig. 3, six time traces of the data sampled by the CTS receiver are shown. The data shown in the two upper plots (a), (b) are from channels centered around 110.5 GHz and 110.9 GHz, 0.5 GHz, and 0.9 GHz away from the gyrotron line, respectively. Referring to Fig. 2, the channels are expected to be subject to scattered radiation arising from the bulk ions (0.5 GHz) and the fast ions (0.9 GHz). The blue curve sections represent the signal level during the time when the gyrotron is switched off (ECE) while the red corresponds to the signal during the gyrotron probing time (ECE+CTS). Here the term ECE covers both the ECE background emitted from the plasma and the receiver noise. We refer to the periods when the probe is on (off) as gyro periods (ECE periods). The time gaps between the gyro and ECE periods are due to the pin switch discussed above. In order to extract the CTS signal the ECE level must be estimated in the gyro periods. To this end, the ECE signal is monitored some GHz away from the gyrotron frequency at both higher and lower frequencies. Here no scattered signal is present. These data are shown in the two lower plots in Figs. 3(e) and 3(f). These signals combined with the ECE level recorded in the ECE periods in channel n are used to give an estimate of the ECE level during the gyro periods in channel n. The estimated ECE levels are shown as green curves in all plots in Fig. 3. As a demonstration of the robustness of the ECE fitting, a channel where no signal is expected (108.98 GHz) is also presented in the figure. The extracted scattered signal level from this channel using the ECE fitting averages out to zero and has a standard deviation less than 0.5 eV for samples integrated over one gyro period of 2 ms. This includes uncertainty due to both the stochastic nature of the ECE and noise signal and the uncertainty in the ECE fitting.

In shot No. 89509 a scattering geometry was established having an overlap at a position of $R=1.67\ \mathrm{m}\pm0.08$ m, $z=0\mathrm{m}\pm0.03$ m. The wave vector of the resolved fluctuation made an angle of 113° to the magnetic field. These values are estimated by ray tracing. Ion heating was provided by 1.3 MW of cocurrent neutral-beam injection with an acceleration voltage of 53 keV and 1 MW of ion cyclotron resonance heating at 38 MHz. Both were applied until $t=2.2$ s. After the main heating phase the ECE background can be seen to decrease over approximately 50 ms in Fig. 3. During the heating phase, sawtooth oscillations are seen at $t=1.97$ s, $t=2.05$ s, $t=2.14$ s, and $t=2.23$ s in the electron temperature time traces from the ECE diagnostics and electron density time traces from the interferometer. These sawtooth oscillations are seen as sudden increases in the ECE background in the CTS data in Fig. 3, due to ECE emitted from the edge of the plasma and not the plasma center. Despite the strong perturbation of the ECE background at sawtooth crashes, no evidence of sawtooth oscillation is seen in the CTS signal centered at a frequency of 110.9 GHz as shown in Fig. 4. The 110.5-GHz channel, however, shows a clear sawtooth response. Other CTS channels also see the sawtooth oscillation as shown in Fig. 4. A contour plot of 21 CTS channels is given in Fig. 5. A clear effect on the spectra can be seen when the ion heating is turned off at 2.2 s. The spectra during the heating flat top ($t=2.1$ s) and 100 ms after the turn off ($t=2.3$ s) are also shown. For this discharge the number of channels for which data were recorded was limited by the number of available analog to digital converters (ADCs). The signal from the fast ions was expected to be at frequencies higher than the gyrotron frequency. Hence, the channels recorded were selected so that there were no spectral gabs from 110.14 GHz to 111.18 GHz, unlike the situation below 110 GHz. In the rest of the discharges shown here more ADC's were available and no such prioritization was necessary.

We will return to this discharge later where the spectral evolution and the corresponding velocity distribution will be discussed in more detail.

IV. EVIDENCE OF THE CTS ORIGIN

In the upgraded diagnostic [23,24] the viewing direction of the receiver beam can be scanned more than 10° per sec-

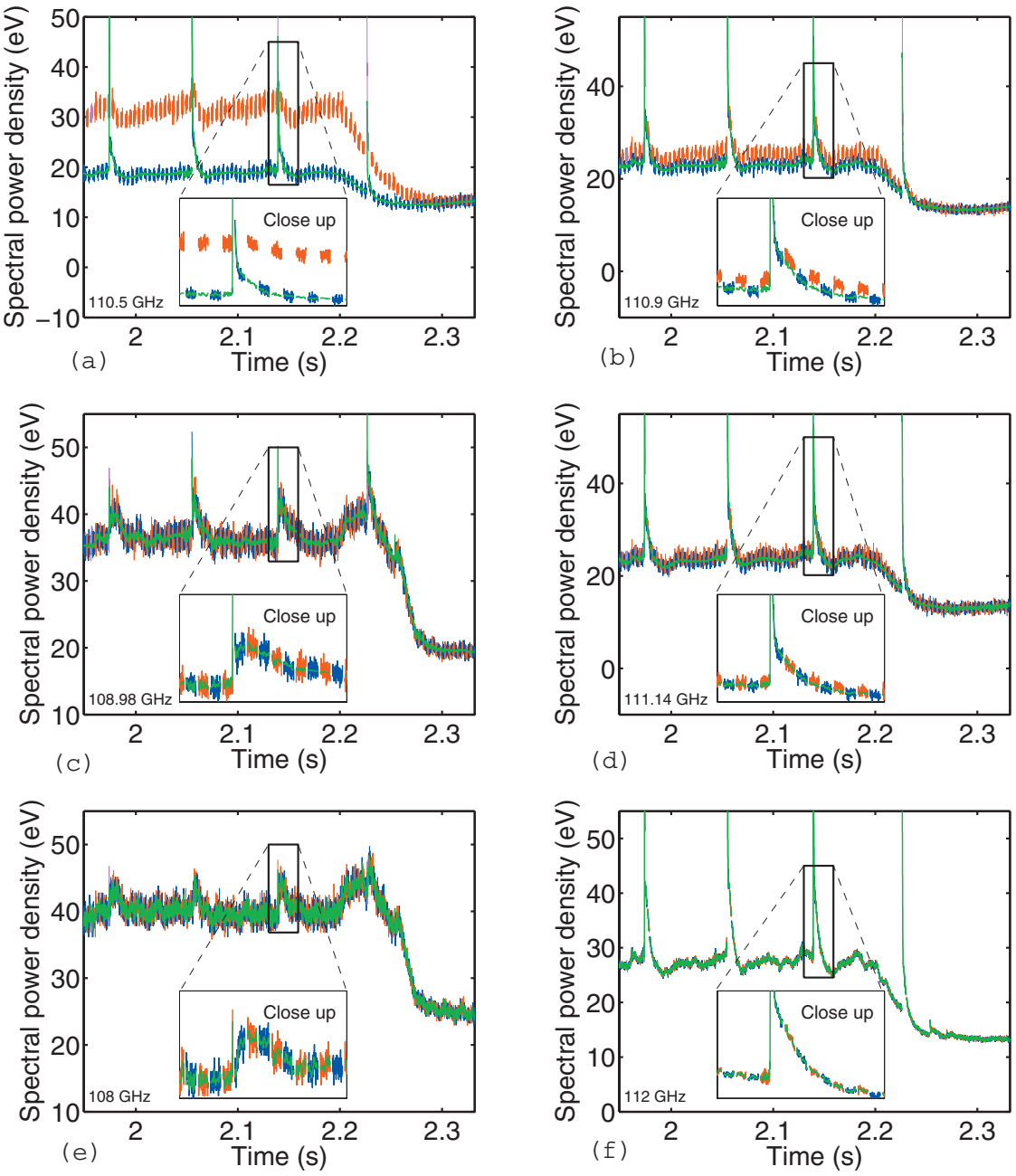

FIG. 3. (Color) Time trace of raw data sampled in six different channels. Red curves represent samples taken during gyro periods (gyrotron on, CTS+ECE), while blue are samples taken during ECE periods (gyrotron off, ECE). In the two upper plots (a), (b) the CTS component of the signal is visible. The two lower graphs (e), (f) show data from frequency channels where no CTS signal is expected. The green line is the reconstructed ECE level during the gyro periods. (c) shows a channel where no CTS signal is expected and in (d) only a small CTS level is expected. It is seen that the background ECE of all the channels have a similar temporal behavior including a strong perturbation due to sawtooth crashes at times 1.97 s, 2.05 s, 2.14 s, and 2.23 s.

ond permitting a wide scan of viewing direction within the duration of a plasma discharge. Such scans facilitate finding overlap between probe and receiver beam. They also provide good evidence that the signals attributed to CTS are genuine and not due, for instance, to spectral impurity of the gyrotron emission, as seen in the recently published results from the Frascati Tokamak upgrade (FTU) CTS [28]. An example of such a scan is shown in Fig. 6. Here the viewing direction of the receiver beam was scanned toroidally, passing through the fixed probe beam. The gyrotron was modulated with a duty cycle of 5% (2 ms on, 38 ms off). The probe beam was launched in the horizontal midplane with a toroidal angle of −10° to the poloidal plane (positive in the clockwise direction as seen from above) and the receiver toroidal angle was swept from −20° to 0° while having a close to constant elevation angle of −26° relative to the horizontal plane (i.e., looking downwards, as in Fig. 1). The result of the scan is shown in Fig. 6. A clear signal is seen to appear with a maximum at 2.1 s. Since the receiver mirror is located approximately 50 cm from the scattering volume and the over-

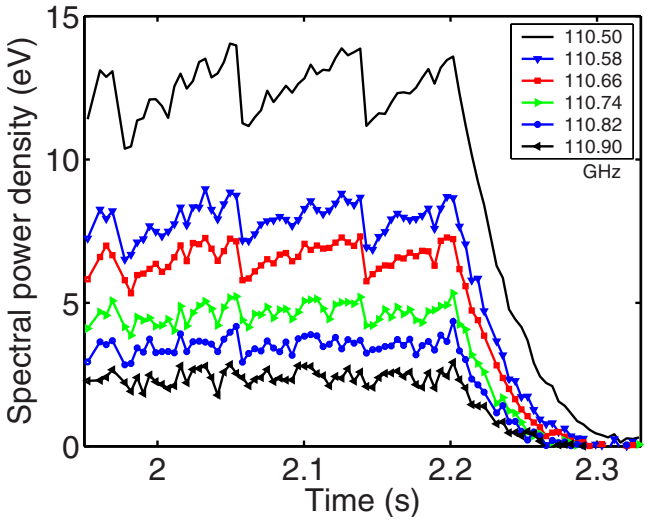

FIG. 4. (Color online) Spectral power density in six CTS channels during TEXTOR shot No. 89509.

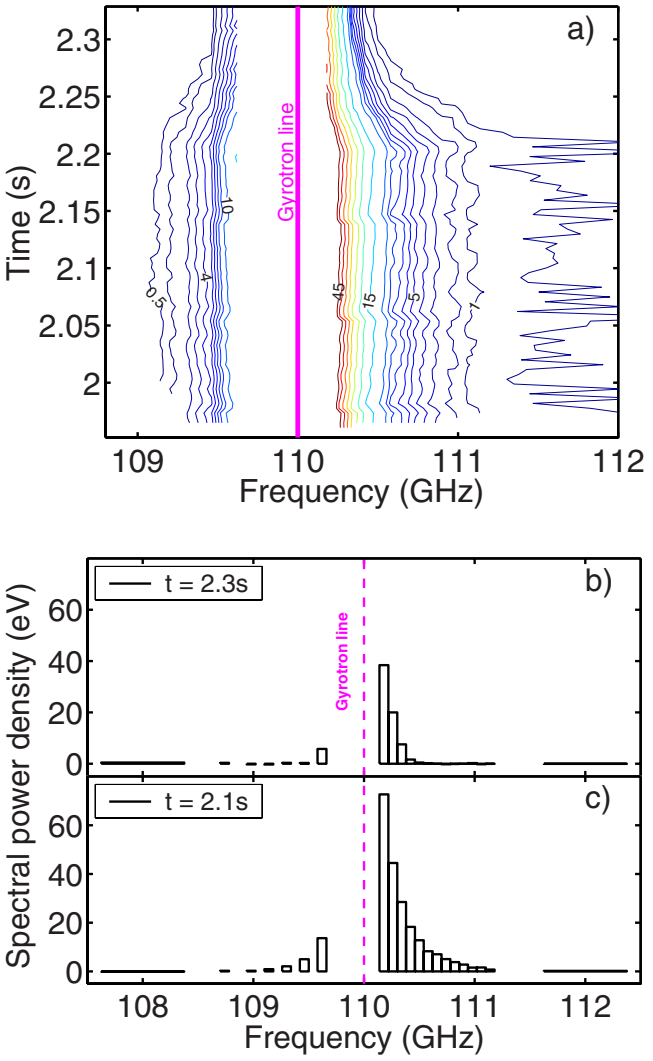

FIG. 5. (Color online) Contour plot of CTS spectral power density (a). The width of the CTS spectrum is seen to decrease after the ion heating is turned off at $t=2.2$ s. CTS spectrum at $t=2.3$ s (after heating turn off) is shown in the upper plot (b) while that at $t=2.1$ s (during heating flattop) is shown in the lower plot (c).

lap is seen from the graph to be present within 5° of the toroidal receiver angle, it follows that the toroidal width of the widest of the probe and receiver beams is approximately 4 cm, in agreement with the expected widths of the probe and receiver beams in the overlap region. This is then also an approximate upper limit on the extent of the scattering volume in the direction orthogonal to the probe and receiver beams.

Another demonstration that the measured data are the result of CTS and carry information on ion dynamics, and that they are not an artifact of spectrally impure gyrotron emission, can be seen in Figs. 7 and 8 where CTS measurements from two similar plasmas with coinjected neutral beam are presented for two different scattering geometries, one viewing in the codirection, the other in the counterdirection, respectively. In both cases a central scattering volume was established at $R=1.8$ m.

In plasma shot No. 97984 (Fig. 7) the resolved fluctuation wave vector $\mathbf{k}^{\delta}$ has an angle to the static magnetic field of ~45°. It is seen than the CTS spectra are unsymmetrical during the heating phase (until $t=4.5$ s), extending to frequencies lower than the gyrotron frequency indicating that $\mathbf{v}_{\text{fast ions}}\cdot\mathbf{k}^{\delta}<0$ [see geometry in Fig. 7(b)]. This agrees with the fact that the birth velocity of the beam injected fast ions is antiparallel to the magnetic field.

Likewise, in plasma shot No. 100911 (Fig. 8), the resolved angle is $\angle(\mathbf{k}^{\delta},\mathbf{B}_0)\approx 135°$ and a positive frequency shift is dominating the CTS spectra during the beam-heating phase until $t=4.0$ s. Here sawtooth oscillations are seen to perturb the CTS spectra. A detailed analysis of the fast-ion interaction with sawtooth oscillation measured by CTS will be addressed elsewhere.

V. INFERRING THE VELOCITY DISTRIBUTION

The CTS spectrum depends on a range of plasma parameters. Most important for the spectra considered in this paper is the fast-ion distribution, but for frequencies closer to the gyrotron frequency other parameters, such as electron density, bulk ion temperature, and impurity ion concentration, have dominant influence on the spectra. Plasma turbulence is in principle also contributing to the spectra but at frequencies which are masked by the notch filter. The parameters which the spectra depend on, but which are of secondary interest, are referred to as nuisance parameters. Some of the nuisance parameters are known from other diagnostics with a finite uncertainty. The measured CTS spectra are fitted using a least-squares fitting procedure which takes prior information about parameters, in particular nuisance parameters, into account and implements a Bayesian method of inference where information from a range of diagnostics is combined optimally with the information provided by the CTS diagnostic [29]. In the Bayesian terminology the applied procedure is that information about parameters from diagnostics other than CTS is represented by a distribution function called the prior. The information on parameters provided by CTS is

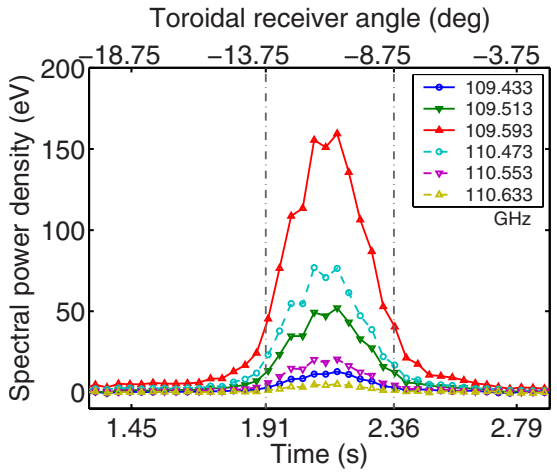

FIG. 6. (Color online) TEXTOR shot No. 100467. Toroidal scan of the receiver beam viewing direction during an Ohmically heated plasma discharge. The probe beam was injected in the horizontal midplane with a toroidal angle of −10°. The receiver beam is seen to intersect the gyrotron beam in the time from 1.91 s to 2.36 s corresponding to a toroidal receiver angle of −13.75° to −8.75°. The scattering position was located at $R=1.8$ m, $z=0$ m and gave rise to an angle of 110° between the magnetic field and the wave vector of the resolve fluctuations (i.e., close to perpendicular to **B**).

represented by a distribution function called the likelihood function. The product of the prior and the likelihood is the posterior and represents the combined information from all involved diagnostics. The maximum of the posterior is the best estimate provided from the least-squares fitting procedure employed here. This approach, least squares with nuisance parameters (LSN), is discussed in more detail in Ref. [29]. The forward model used in the inference is a fully electromagnetic model of CTS with magnetized thermal ions while the fast ions are treated as unmagnetized [15].

The ion velocity distribution is assumed to consist of a thermal part and a superthermal part. The thermal bulk ions consist of Maxwell-distributed populations of deuterons and protons. Impurity ions are represented by Maxwell-distributed carbon and iron. Bulk and impurity ions are assumed to be in thermal equilibrium and are characterized by density, temperature, and a drift velocity along the magnetic field. The scattering geometries realized in the presented discharges are not sensitive to a poloidal rotation, which is thus not included in the model. The fast-ion population is modeled by a one-dimensional (1D) distribution function defined by a number of velocity nodes through which a smoothed trapezoidal function is drawn. An example of an ion distribution model optimized to fit the measured data is shown in Fig. 9(b). The plot shows the tail of the bulk deuteron and proton distributions plotted together with the fast-ion velocity nodes (dots) defining the fast-ion distribution function. The resulting spectrum and the measured data, the latter represented by a histogram, are shown in Fig. 9(a). No data are present in the vicinity of the probing frequency due to the notch filter. The fluctuations induced by the impurity and bulk ions dominate the central part of the CTS spectrum which is monitored by seven CTS channels in this example.

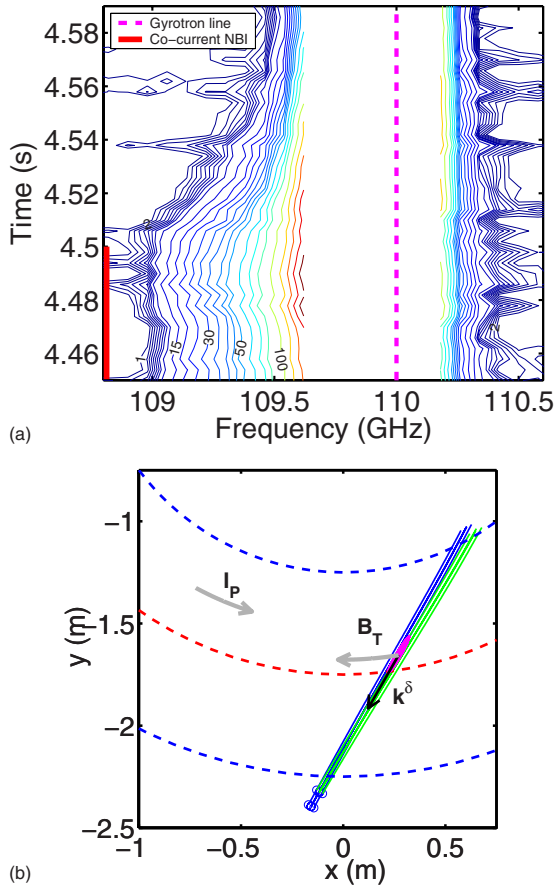

FIG. 7. (Color online) (a) CTS signal for a central overlap in the horizontal midplane with $\mathbf{B}_T\cdot\mathbf{k}^\delta>0$ and $\mathbf{I}_p\cdot\mathbf{k}^\delta<0$. A clear signature of the beam is seen in the spectral power density. The neutral beam injection (NBI) is turned off at $t=4.5$ s. The overlap geometry (top view) is shown in (b).

The shape of this part depends on seven parameters: n_e, T_e, n_D/n_H, T_i, drift velocity, and the two impurity concentrations. Most of these parameters are well diagnosed by other systems reflected in a prior distribution function with small width with respect to these parameters. This makes it possible to extract estimates of the ion temperature and drift velocity from the CTS data if prior information of these are not included. Finally, for frequencies greater than 110.5 GHz the fast-ion feature is seen to dominate.

The prior information may affect the error bars associated with the inferred velocity distribution. The spectral variations as functions of the beam overlap and incident power [see the equation of transfer Eq. (1)] is that of a single scaling factor. Before any data treatment the scaling factor is poorly known. This is because estimates of the total probing power and the beam overlap are uncertain. The data analysis is divided into two parts. In the first step, the prior of the scaling factor is very broad reflecting large uncertainty in our knowledge of this value. Based on the assumption that the scaling factor is a constant for all recorded CTS spectra in a discharge the scaling factor can be estimated with a much reduced uncertainty. This information is represented by a new prior with much reduced width. The error bars shown in Fig. 10(a) represent the uncertainties in the inferred fast-ion velocity

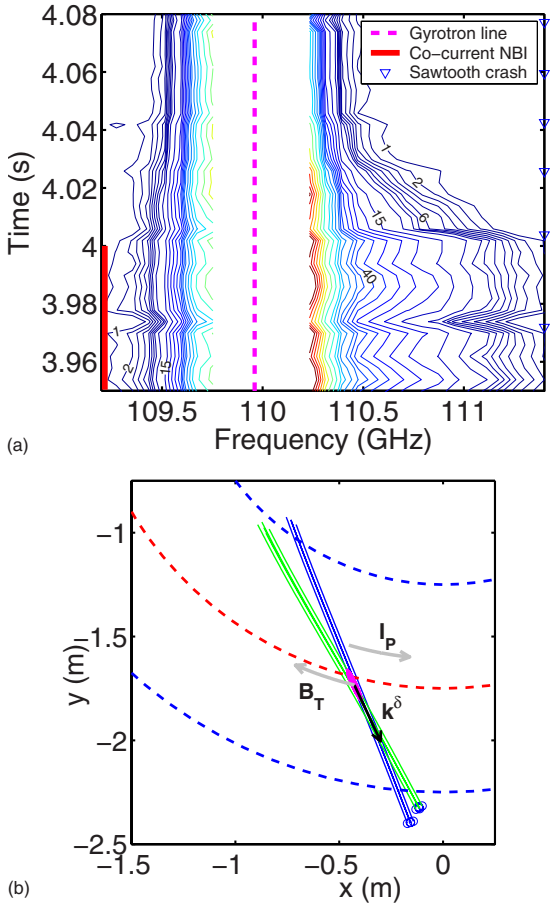

FIG. 8. (Color online) (a) CTS signal for a central overlap in the horizontal midplane with $\mathbf{B}_T \cdot \mathbf{k}^\delta < 0$ and $\mathbf{I}_p \cdot \mathbf{k}^\delta > 0$. Here sawtooth oscillation are present at times 3.972 s, 4.004 s, 4.026 s, 4.043 s, 4.060 s, and 4.077 s. The overlap geometry (top view) is shown in (b).

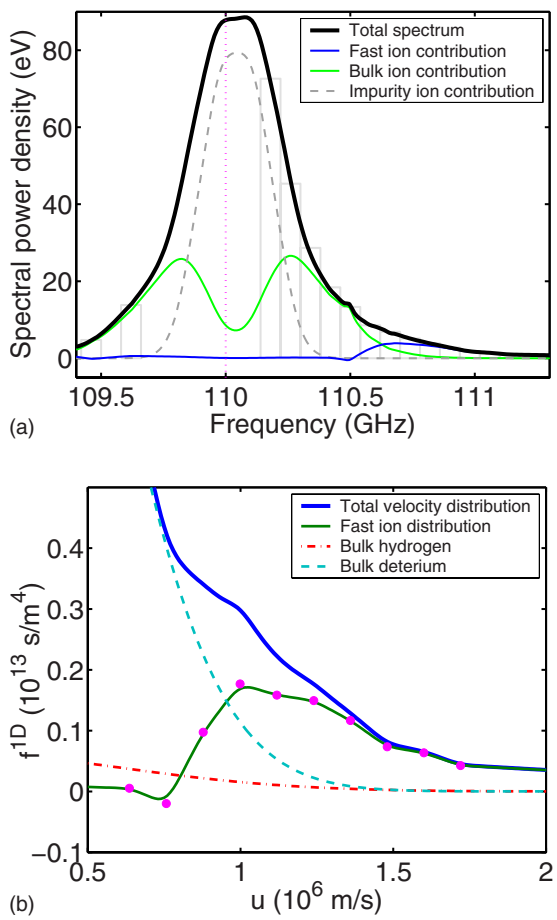

FIG. 9. (Color online) Outcome of an LSN fit to the measured data. (a) Measured data overlayed with theoretical model. (b) Model distribution. The dots are the nodes defining the fast ion distribution represented by the full curve. The bulk deuterium and hydrogen distributions are represented by dashed curves.

distribution obtained using the original prior for scaling factor and the impurity concentrations. The reduced error bars in Fig. 10(b) result from the use of the new narrower prior for scaling factor and impurities concentrations—i.e., making use of the assumption that these parameters are near constant throughout the CTS recording period.

VI. DISCUSSION OF INFERRED VELOCITY DISTRIBUTIONS

The inferred velocity distribution for plasma discharge No. 89509 is shown in Fig. 11. There is asymmetry in the distribution which is due to the beam ions injected in the codirection and the scattering geometry is such that the resolved direction in velocity space has a component in the codirection. At the heating turnoff the distribution is seen to relax towards a pure Maxwell distribution with a lower temperature. Also the plasma drift velocity can be seen to change. Before the turnoff the plasma is seen to rotate in the direction of the beam injection. Just after the turnoff the distribution gets centered closer to zero velocity.

A set of 1D slices of Fig. 11 are presented in Fig. 12. Here the time evolution at four velocities is shown. It may be seen that sawtooth oscillations are present at velocities close to the bulk distribution (0.5×10^6 m/s) while no clear evidence of sawtooth behavior is seen in the superthermal velocity nodes in this discharge. Two time slices are also shown in the figure. Here the bulk part is plotted along with the fast-ion distribution. It can be noted that at $t=2.1$ s a significant nonthermal part is present while at $t=2.3$ s the shape is purely Maxwell distributed.

TEXTOR has the capability of changing the neutral beam power without changing the acceleration voltage. This is done by changing the V target of the injector and thereby scraping off a part of the beam [30]. The velocity distribution was measured during two discharges with different injected power (0.4 MW and 1.0 MW) but with constant acceleration voltage of 50 keV. In both cases hydrogen atoms were injected into a hydrogen plasma. In the two discharges, a CTS measurement was performed 700 ms after the beam turnon. The scattering volume was located near the plasma center ($R=1.81$ m), and the resolved fluctuation wave vector had an angle of 140° to the magnetic field. Both discharges had a central electron density of 2.4×10^{19} m^{-3} in the CTS time window while the electron temperature measured by Thomson scattering and ECE diagnostics was 1.5 keV in the low-

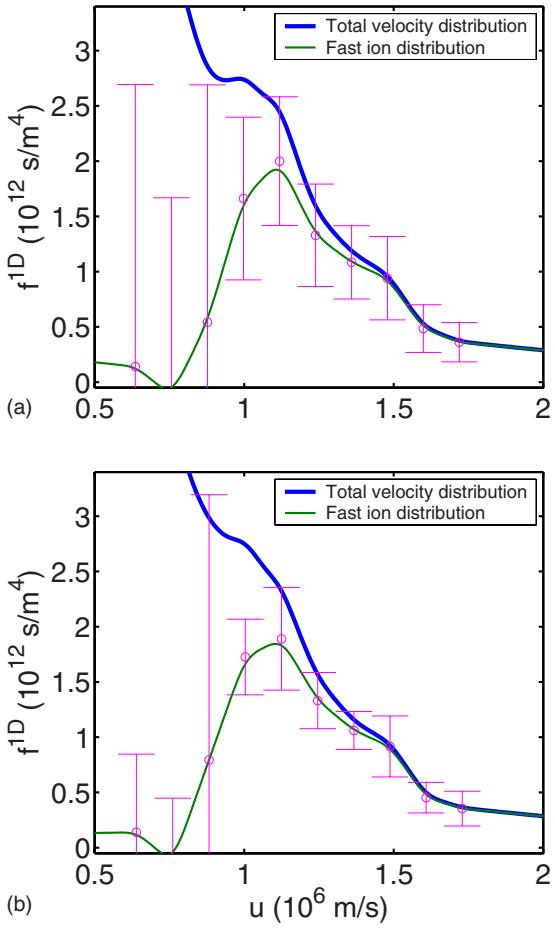

FIG. 10. (Color online) Fast-ion velocity nodes with error bars using a broad prior (a) and a new prior with reduced width (b) assuming that the scaling and the impurity levels are near constant throughout the CTS measuring time.

beam-power discharge and 1.9 keV in the high-power discharge. The ion temperature is estimated from charge exchange spectroscopy to be 1.1 keV and 2.0 keV in the plasma center, respectively. The measured spectra are shown in Fig. 13. The inferred fast-ion velocity distributions are displayed in Fig. 14. It can be seen that even though the change in beam power is 150% the fast particle contribution is increased by a factor of 3. Since the electron and ion temperatures are measured to be higher in the high-beam-power discharge, the fast ion slowing down rate will be lower. This, combined with the difference in influx of injected fast particles, explains the difference seen in the superthermal part of the distributions. Fokker-Planck simulations of these discharges have been performed and are also presented in Fig. 14.

VII. COMPARING WITH NUMERICAL SIMULATION

We model the fast ions and the bulk ions using the Fokker-Planck equation [31] for a homogeneous plasma. This allows us to simulate the behavior of a small population of energetic test particles and compare the evolution of these with the CTS fast-ion measurements taken near the center of

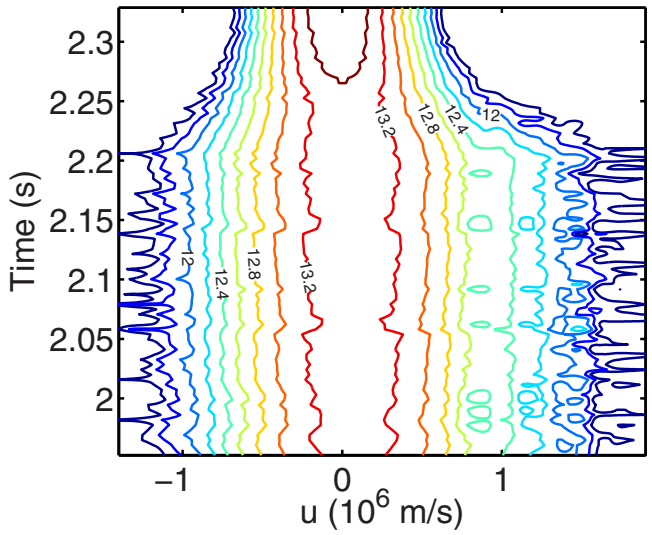

FIG. 11. (Color online) Log_{10} contour plot of obtained velocity distribution. The scattering geometry is described in Sec. III with a radial position of $R=1.67$ m and a resolved direction of 113° to the magnetic field.

the plasma. In the center of TEXTOR, the energetic ion trajectories generally remain close to the plasma center. This justifies the use of a homogeneous plasma.

The Fokker-Planck simulation uses the electron density measured by interferometry and the electron temperature from ECE and Thomson scattering diagnostics as input. The fast-ion source term is given by a neutral beam source term

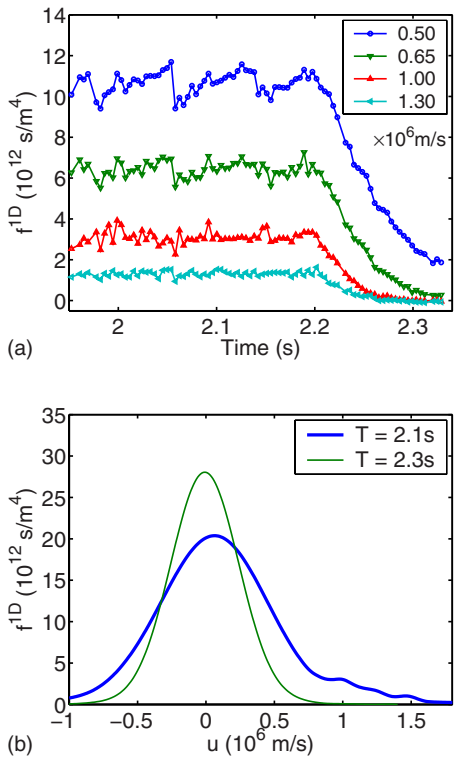

FIG. 12. (Color online) (a) Time traces of the velocity distribution. (b) Time slices of the velocity distribution.

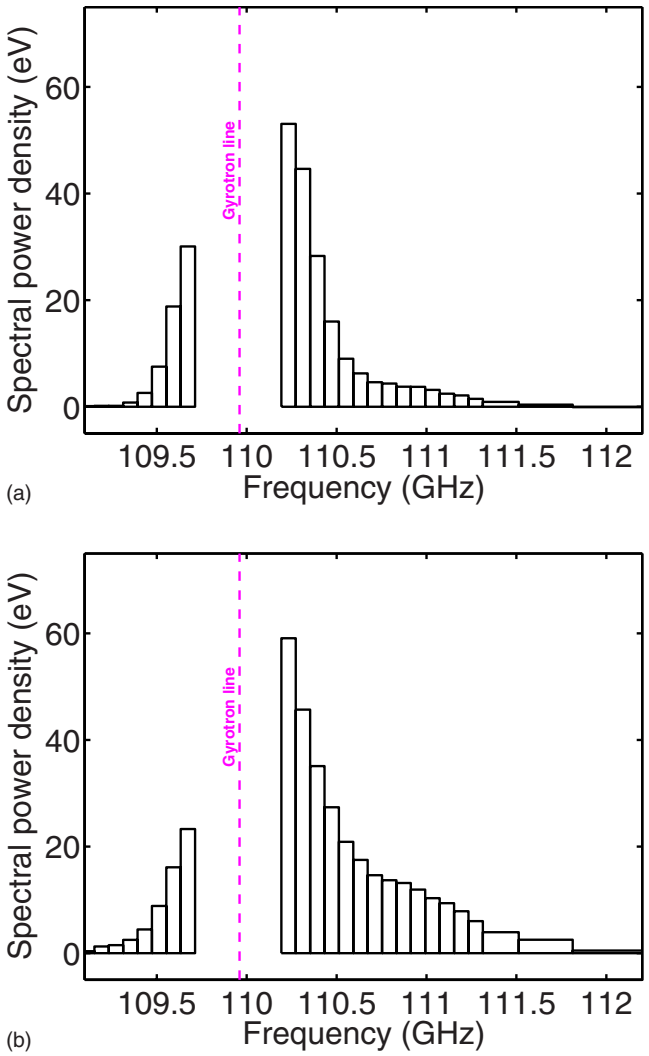

FIG. 13. (Color online) Measured spectrum for discharge with low injected beam power (a) and with high injected beam power (b).

where the total input power has been divided up into three energy peaks, representing the birth energies E, $E/2$, and $E/3$, where $E=50$ keV. In the TEXTOR neutral-beam injectors this ratio is $(R_E, R_{E/2}, R_{E/3})=(0.33, 0.42, 0.26)$ for hydrogen injection and (0.41, 0.38, 0.21) for deuterium injection at an acceleration voltage of 50 keV [32]. The beam deposition rate is calculated taking the ionization rate of the neutrals to be proportional to the local density and integrating along the beam injection path. No effect of the ICRH is included in the source term. The computed bulk ion temperature and drift are the results of interaction with the electrons and the fast ions and loss of energy and momentum through transport. Test particles with a velocity above the critical velocity [33] v_c are primarily slowed down due to interaction with electrons, while below v_c the bulk ions are dominating the interaction. In the TEXTOR plasmas considered in this paper, v_c in the plasma center spans $1.8-2.2\times10^6$ m/s. Since the main part of the measured nonthermal ions have velocities lower than this, the energy loss of the test particles is mainly transferred to the bulk ions. The test particle momentum loss

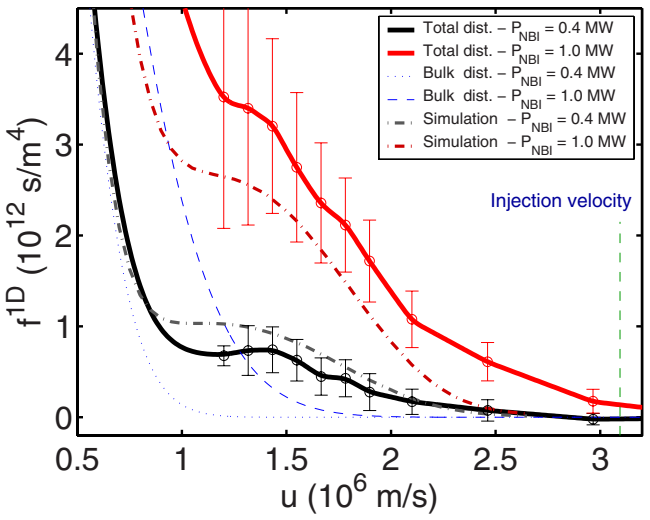

FIG. 14. (Color online) Measured velocity distribution and overlayed Fokker-Planck simulation velocity distribution for different injected beam power for constant acceleration voltage. In both discharges the scattering volume was located at $R=1.81$ m. The resolved direction was 140° to the magnetic field.

is transferred to the bulk plasma driving the plasma rotation. The ion temperature is furthermore asymptotically approaching the electron temperature. The electron temperature is given as an input. Additionally, an energy loss term and a momentum loss term is added intended to represent transport away from the hot plasma center. The loss terms are represented by confinement times for ion energy and momentum (250 ms and 45 ms, respectively), both of which are set for the best fit in the flat top period and are as such purely *ad hoc* parameters. Their values are kept constant throughout the modeling including the slowing-down period. The bulk particle confinement time is set to match the measured density. The test particles evolve towards a Maxwell distribution in equilibrium with the bulk ions and electrons. Once the energetic test particles have slowed down, they are transferred to the bulk population. This is done by extracting and transferring the fraction of the test population which has the same distribution as the bulk. This maintains the condition

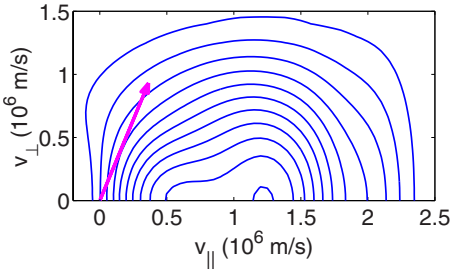

FIG. 15. (Color online) Fokker-Planck simulation of beam ions for TEXTOR shot No. 89509 at the NBI flat top at $t=2.1$ s. The contour levels are equispaced. The cylindrical coordinates $v_\parallel$ and $v_\perp$ represent the direction antiparallel and perpendicular to the static vacuum magnetic field. The direction of the projection measured by CTS, 67° to $v_\parallel$, is indicated by the arrow.

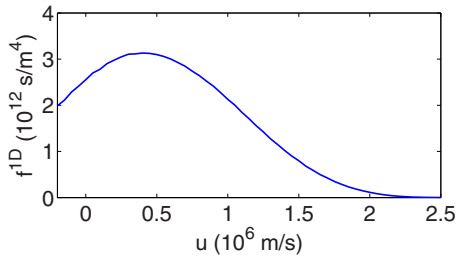

FIG. 16. (Color online) Projection of the simulated energetic-ion test population shown in Fig. 15.

that the test particle density is small compared to the bulk density.

A contour plot of the simulated fast-ion distribution during neutral-beam injection in TEXTOR shot No. 89509 is shown in Fig. 15 at a time where a stationary solution has been established. The resolved direction measured by CTS is indicated in the figure. The projected 1D fast-ion distribution function of this Fokker-Planck simulation is presented in Fig. 16.

As mentioned above, the source term only takes beam ions into account although the experiment also had ion cyclotron resonance heating. The resonance of the ion cyclotron heating was, however, located on the low-field side and is assumed not to influence significantly the fast ions in the scattering volume, which was placed slightly on the high-field side of the center.

The time evolution of the projected ion distribution obtained from the simulation is presented as a $\log_{10}$ contour plot in Fig. 17. The projection includes both the energetic test particles and the bulk-ion distribution. Inferred and modeled velocity distribution is compared at three superthermal velocities in Fig. 18. The simulated data are seen to agree well with the measured velocity distributions shown in Fig. 19. In both the simulation and the experiments the heating

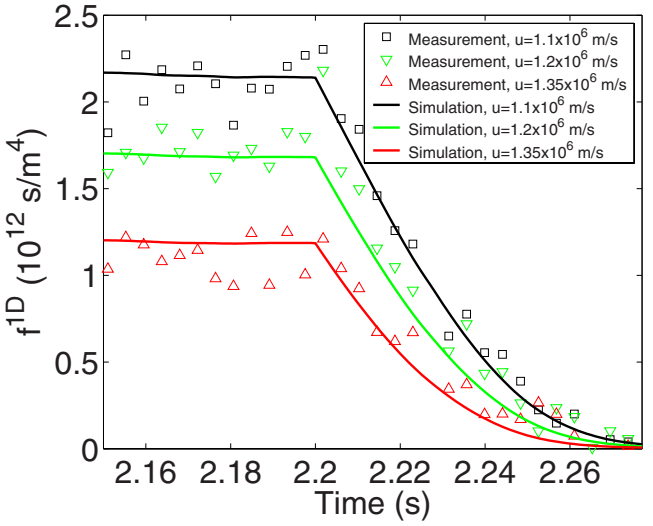

FIG. 18. (Color online) Direct comparison of measurement and simulation at superthermal velocities. As shown in Fig. 9(b) the ion population densities at $u=1.1$, 1.2 and 1.35×10^6 m/s extend the bulk distribution. Good agreement during the slowing-down phase is found.

was turned off at 2.2 s, giving rise to decay of the population of fast ions with velocities in the range $1-1.5\times10^6$ m/s. The middle part of the measured distribution, from -0.6 to 0.6×10^6 m/s, is governed by the ion temperature and is associated with some uncertainty since only a few frequency channels were covering the bulk ion spectral features. Despite the limitations described in the in the beginning of the section, a satisfactory agreement is seen between the measured and simulated fast ions. It is seen that the decay of the fast ions is described well by a classical slowing down.

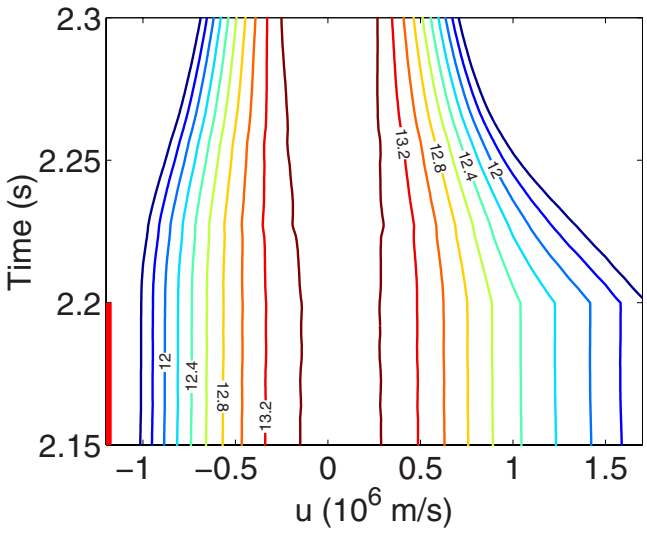

FIG. 17. (Color online) Time evolution of the 1D projected Fokker-Planck simulation of beam ions for TEXTOR shot No. 89509 ($\log_{10} f^{1D}$).

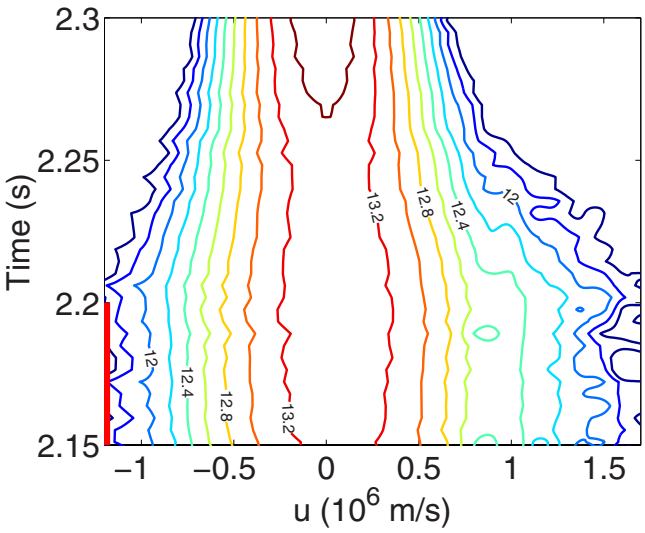

FIG. 19. (Color online) Time evolution of the measured 1D velocity distribution ($\log_{10} f^{1D}$). The fast ions seen at $u=1-1.5\times10^6$ m/s decay once the ion heating is turned off at t=2.2 s.

VIII. CONCLUSION

In conclusion, we have shown measurements of the temporal evolution of fast-ion velocity distributions obtained by collective Thomson scattering. Examples of data are presented which give good evidence that the signals are indeed due to CTS and that valuable estimates of the fast-ion velocity distributions can be inferred from them. The relaxation of the ion velocity distribution after switch off of auxiliary heating was inferred from CTS and agreed remarkably well with simple Fokker-Planck simulations. These results represent a breakthrough for the use of millimeter-wave collective Thomson scattering for diagnosing dynamics of confined fast ions in fusion plasmas and constitute an important milestone in preparing this diagnostic technique for use at ITER.

ACKNOWLEDGMENTS

The authors would like to thank the TEXTOR team, the TEC ECRH team, and the TEC ICRH team. This work was supported by EURATOM and U.S. DOE.

[1] M. Rosenbluth and P. Rutherford, Phys. Rev. Lett. **34**, 1428 (1975).
[2] C. Cheng and M. Chance, Phys. Fluids **29**, 3695 (1986).
[3] V. S. Belikov, Y. I. Kolesnichenko, and V. V. Lutsenko, Nucl. Fusion **35**, 207 (1995).
[4] W. Kerner, D. Borba, S. Sharapov, B. Breizman, J. Candy, A. Fasoli, L. Appel, R. Heeter, L. Eriksson, and M. Mantsinen, Nucl. Fusion **38**, 1315 (1998).
[5] K. Wong, Plasma Phys. Controlled Fusion **41**, R1 (1999).
[6] M. Isikawa *et al.*, Nucl. Fusion **60**, 1474 (2005).
[7] D. J. Campbell *et al.*, Phys. Rev. Lett. **60**, 2148 (1988).
[8] J. Graves *et al.*, Plasma Phys. Controlled Fusion **47**, B121 (2005).
[9] Y. Kolesnichenko, V. Lutsenko, R. White, and Y. Yakovenko, Nucl. Fusion **40**, 1325 (2000).
[10] H. Duong and W. Heidbrink, Nucl. Fusion **33**, 211 (1993).
[11] F. B. Marcus, J. M. Adams, D. S. Bond, M. A. Hone, P. J. A. Howarth, O. N. Jarvis, M. J. Loughlin, G. J. Sadler, P. Vanbelle, and N. Watkins, Nucl. Fusion **34**, 687 (1994).
[12] A. Sitenko and Y. Kirochkin, Sov. Phys. Usp. **9**, 430 (1966).
[13] R. Aamodt and D. Russel, Nucl. Fusion **32**, 745 (1992).
[14] H. Bindslev, Plasma Phys. Controlled Fusion **35**, 1615 (1993).
[15] H. Bindslev, J. Atmos. Terr. Phys. **58**, 983 (1996).
[16] H. Bindslev, *Proceedings of the Third International Workshop on Strong Microwaves in Plasmas* (Russian Academy of Sciences, Nizhny Novgorod, 1996), Vol. 1, pp. 109–128.
[17] R. Behn, D. Dicken, J. Hackmann, S. A. Salito, M. R. Siegrist, P. A. Krug, I. Kjelberg, B. Duval, B. Joye, and A. Pochelon, Phys. Rev. Lett. **62**, 2833 (1989).
[18] E. Suvorov *et al.*, Plasma Phys. Controlled Fusion **37**, 1207 (1995).
[19] J. Hoekzema, H. Bindslev, J. Egedal, J. Fessey, C. Gatcombe, N. Hammond, T. Hughes, J. Machuzak, J. Oosterbeek, P. Roberts, A. Stevens, and P. Stott, Rev. Sci. Instrum. **68**, 275 (1997).
[20] P. Woskoboinikow, D. R. Cohn, and R. J. Temkin, Int. J. Infrared Millim. Waves **4**, 205 (1983).
[21] H. Bindslev, J. A. Hoekzema, J. Egedal, J. A. Fessey, T. P. Hughes, and J. S. Machuzak, Phys. Rev. Lett. **83**, 3206 (1999).
[22] H. Bindslev, S. K. Nielsen, L. Porte, J. A. Hoekzema, S. B. Korsholm, F. Meo, P. K. Michelsen, S. Michelsen, J. Oosterbeek, E. L. Tsakadze, E. Westerhof, and P. Woskov, Phys. Rev. Lett. **97**, 205005 (2006).
[23] S. Michelsen, S. Korsholm, H. Bindslev, F. Meo, P. Michelsen, E. Tsakadze, J. Egedal, P. Woskov, J. Hoekzema, F. Leuterer, and E. Westerhof, Rev. Sci. Instrum. **75**, 3634 (2004).
[24] S. Korsholm *et al.*, Rev. Sci. Instrum. **77**, 10E514 (2006).
[25] H. Bindslev, L. Porte, A. Hoekzema, J. Machuzak, P. Woskov, and D. Van Eester, in *Proceedings of the 26th EPS Conference on Controlled Fusion and Plasma Physics, Maastricht, 1999*, edited by R. Pick (European Physical Society, Paris, 1999), Vol. 23J, pp. 765–768.
[26] H. Bindslev, L. Porte, A. Hoekzema, J. Machuzak, P. Woskov, D. Van Eester, J. Egedal, J. Fessey, and T. Hughes, Fusion Eng. Des. **53**, 105 (2001).
[27] L. Porte, H. Bindslev, F. Hoekzema, J. Machuzak, P. Woskov, and D. Van Eester, Rev. Sci. Instrum. **72**, 1148 (2001).
[28] U. Tartari *et al.*, Nucl. Fusion **46**, 928 (2006).
[29] H. Bindslev, Rev. Sci. Instrum. **70**, 1093 (1999).
[30] R. Uhlemann and J. Ongena, Fusion Technol. **35**, 42 (1999).
[31] M. N. Rosenbluth, W. M. Macdonald, and D. L. Judd, Phys. Rev. **107**, 1 (1957).
[32] R. Uhlemann (private communication).
[33] W. W. Heidbrink and G. Sadler, Nucl. Fusion **34**, 535 (1994).